Measurement of Atmospheric Icing and Droplets

Stefani Rydblom, *Member, IEEE*, and Benny Thörnberg

***Abstract*— Icing conditions including atmospheric liquid water content (LWC) and size distribution of droplets were recorded close to the top of Mt. Åreskutan, 1260-m above sea level, Sweden, a place known for frequent severe icing. The findings are comparatively analyzed. Combitech IceMonitor was used to measure the ice load, and HoloOptics T41 was used to measure the atmospheric icing rate. A method to translate the digital output from HoloOptics T41 to a value between 0 and 100 is described and used. Two instruments were used for measuring LWC and the median volume diameter (MVD). We created a model of icing intensity based on the *k*-nearest neighbor (KNN) using wind speed, LWC, and MVD as input. The result indicates that more learning data decrease the error. An heuristic model of erosion/ablation was added to simulate the ice load, and the result was compared with that of the standard Makkonen ice load model. The Makkonen model is suitable for estimating the ice load using a 1-h temporal resolution. With a 1-min temporal resolution, the erosion/ablation needs to be modeled and included. Our observations show that conditions can alternate between icing and erosion/ablation within 1 min during an icing event.**

***Index Terms*— Atmospheric measurements, ice, imaging, instrumentation and measurement, meteorology, weather forecasting.**

I. Introduction

ATMOSPHERIC icing is a persistent problem for wind turbines and many other businesses in cold climates. The growing wind power industry in regions with cold climates is continuously looking for ways to reduce losses caused by icing [1], [2].

An accurate prediction of power losses due to icing is essential for the operation of wind turbines, the business model of power companies, and the planning of other production [3]. Considerable work has been done to understand the physics and nature of icing [4]–[7], but the prediction of icing and ice load is still considered difficult [8], [9]. Despite the years of research, the icing process is not fully understood, and all available instruments have different limitations and uncertainties [10]. For a wind turbine, both the indication of icing and its counterpart, the indication of no ice, are relevant [11].

Manuscript received July 30, 2019; revised December 30, 2019; accepted December 31, 2019. Date of publication January 15, 2020; date of current version June 24, 2020. This work was supported in part by Swedish Energy Agency under Project 37268-1 and in part by the European Union Regional Development Fund through the SMART Project. The Associate Editor coordinating the review process was Huang-Chen Lee. *(Corresponding author: Stefani Rydblom.)*

Stefani Rydblom is with the RISE Research Institute of Sweden, 852 30 Sundsvall, Sweden (e-mail: stefani.rydblom@ri.se).

Benny Thörnberg is with the Department of Electronics Design, Mid Sweden University, 851 70 Sundsvall, Sweden (e-mail: benny.thornberg@miun.se).

Color versions of one or more of the figures in this article are available online at http://ieeexplore.ieee.org.

Digital Object Identifier 10.1109/TIM.2020.2966313

Our purpose is to provide more icing data to the scientific community to confirm the current models of icing and to validate the studied instruments' behavior in severe icing.

There is a need for *in situ* measurements that can be used as an input to the numerical data analysis to improve the calculation and prediction of icing. The liquid water content (LWC) and the median volume diameter (MVD) of supercooled water droplets are essential parameters that are used in current icing models [2], [7].

In 2016, we presented the droplet imaging instrument (DII), a new instrument for the measurement of LWC and MVD. The idea was to use the commercial technology based on shadowgraphy [12] suitable for an instrument that can be used unattended at a fixed location. A comparative study of this instrument and the cloud droplet probe (CDP) from Droplet Measurement Technologies Inc., Longmont, CO, USA, was done at a location with light-icing conditions. Although we visually noted some icing during this initial field study, our lack of instruments prevented us from taking measurements [13].

Measuring any meteorological parameters in conjunction with atmospheric icing has proven to be a challenging task. Ice tends to stick to the instruments, affecting the measurements and eventually causing the instruments to break or fail. Instruments that measure the LWC and the MVD of droplets usually require interaction with the droplets or rely on sensitive optical components and are, thus, prone to failure in very icy conditions. Even instruments that are specifically designed to detect and quantify icing often fail in the iciest conditions, making it challenging to measure LWC and MVD, as well as to quantify the icing in very icy conditions. Still, in order to create mathematical models that can predict icing events accurately, there is a pressing need for more of these measurements.

During the winter of 2018–2019, a measurement station was set up near the peak of Åreskutan, Sweden, at a position 63°25′38″N, 13°4′40″E. The station was equipped with the same two instruments to measure the droplet size and concentration as in previous study. Two other instruments were used to detect icing: IceMonitor from Combitech AB, Östersund, Sweden, and HoloOptics T41, HoloOptics, Stockholm, Sweden. Wind speed, wind direction, temperature, relative humidity, and barometric pressure were measured using the Eolos-Ind Static Weather Sensor (here abbreviated Eolos) from Lambrecht Holzbau GmbH, Schwalmstadt, Germany.

The result confirms the relationship between LWC, MVD, icing rate, and ice load. It shows that the concentration of droplets during an icing event varies and that icing is a process that occasionally includes both accumulation and erosion in cycles as short as 1 or 2 min. It also shows that an accurate estimation of icing for a specific location can be made using

the local *in situ* measurement data in the multivariate data analysis.

A. Scientific Contribution

An efficient operation of wind turbines in regions with cold climates requires the knowledge of when atmospheric icing is happening and its connection with known meteorological parameters. As far as we know, there is no previously published field study on MVD, LWC, and icing on a fixed location with a 1-min temporal resolution.

This article aims to enhance the knowledge on the icing process, the relationship between MVD, LWC, and ice load, the nature of icing, the microstructure of an icing cloud, and the performance of instruments in severe icing.

We hope to encourage the development of new and better instruments for use in icing conditions as well as more measurements and sharing of data in order to create better models for the prediction and estimation of icing. The purpose is also to show that even a small amount of data for a specific location can be used to make a model usable in real-world conditions.

The data collected in this article are publicly available [14].

B. Common Definitions

The IEA Wind has published most of the common definitions related to icing [15], [16]. Atmospheric icing is defined as "the period of time where atmospheric conditions are present for the accretion of ice or snow on structures that are exposed to the atmosphere."

The icing intensity is defined by IEA Wind as the accumulation per time on a structure. In this article, we use a value between 0 and 100 as a measure of the icing intensity. It is based on the output from the HoloOptics T41, which we see sometimes is correlated with the icing rate, given by the Makkonen formula in the units kg m^{-1} min^{-1}.

Accretion is the time when ice is growing, and ablation is when ice is removed through natural means, including melting, erosion, sublimation, and shedding. In this article, we have mainly used the word "erosion" when simulating the loss of weight from the IceMonitor. As shedding of ice is partly stochastic and nonuniform, it is difficult to predict. We did not attempt to include shedding in our simulation.

C. Effect of Icing on Wind Turbines

Icing changes the shape of the aerodynamic profile of the wind turbine blades and makes the turbine less efficient [17]–[19]. To fully understand the process of ice accretion and ablation, and from this estimate, the loss in output power, one has to consider the construction of the wind turbine, e.g., its blade profile, radius, blade thermodynamics, active heating, and several other external natural parameters such as humidity, air pressure, and solar radiation [20]–[22]. The industry drives a continuous development toward better designs and strategies to directly measure and avoid icing [16], [23], [24]. Efforts have been made, e.g., by using scaled models of blade profiles in icing wind tunnels, to investigate the change in the aerodynamic profile by ice accumulated on typical profiles and its effects [25], [26].

II. Materials and Methods

The materials for measuring droplets and other meteorological parameters were the same as those used in the measurement in Klövsjö, 2016–2017 [27]. The Eolos includes sensors for wind speed, wind direction, temperature, humidity, and barometric pressure. The measured wind direction is used as an input to the control and motor that rotates the mast in the direction of the wind. The CDP and DII are briefly described. The instruments for icing detection—HoloOptics T41 and Combitech IceMonitor, are described in more detail.

A. Instruments for LWC and MVD Measurements

Mid Sweden University, Sundsvall, Sweden, developed the DII with the purpose of exploring a robust technique for cost-efficient measurement of droplet size and concentration. The system works by shadowgraph imaging using a high-speed digital camera and LED background illumination. The camera and lens are mounted in an aluminum housing with a heated front glass. Facing the camera in an identical housing is a blue LED that produces a short flash of collimated light directed toward the camera. Particles passing between the camera and the illumination appear as dark shapes against the bright background [12], [13].

The size of an imaged droplet is estimated from a measure of the blackness of the shadow. The LWC is estimated by dividing the volume (or weight) of every detected droplet with its expected sampling volume. The sampling volume depends on the optical depth of field, the background lighting conditions, and the size of the measured droplet [28].

Droplet-size measurements using the DII has been shown to have high accuracy when compared with calibrated samples of polymer spheres [27]. The LWC is calculated by estimating the volume if a particle of corresponding size is in sufficient focus to be sized. The concentration measurement in real-world measurements has been shown to have a systematic difference when compared with another instrument (the CDP) [27].

The CDP works by measuring the light scattered forward by single particles [29]–[31]. A focused laser beam illuminates a small area. The passing droplets can be seen as small spherical lenses that scatter the light. The signature of the scattered light of a defined wavelength and scattering angle can be calculated analytically. Droplets passing within the sampling space will be measured according to their phase signature and counted in a series of predefined size bins.

In order to calculate the LWC from the CDP, it is necessary to know the sampling speed. The LWC is calculated by dividing the total mass of the passing particles with an estimation of the volume of air containing the measured particles. The sampling speed is the sample area of the laser beam multiplied with the speed of the passing air. We estimated the speed of the passing droplets to be equal to the measured wind speed. There was no backup instrument for the wind speed.

A detailed description of the CDP and its limitations can be found in [31]–[33].

In this article, the values from the two instruments are compared. In the simulations and the simulations of icing,

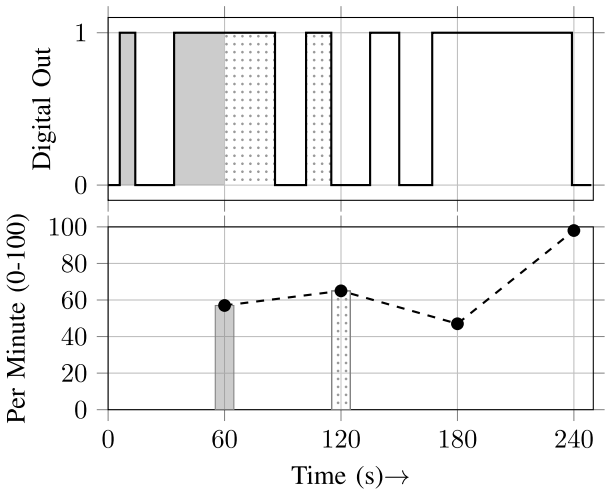

Fig. 1. "Digital Out" shows the output from the sensor. This signal is read every second. "Per Minute" is the accumulated indications per minute in percent.

only the CDP value is used because of its higher sampling rate.

B. Measuring Icing Intensity

The intensity of atmospheric icing caused by supercooled water droplets on a structure can be expressed as a function that is a product of the LWC, the icing efficiency, and the wind speed, where the icing efficiency is mainly determined by the shape and size of the structure, the droplet diameter, and the temperature of the accretion surface [5]. If the structure changes temperature or size due to accumulated ice, the function becomes time-dependent [6].

HoloOptics T41 is an instrument designed to measure the rate of atmospheric icing. It works by measuring the reflectance of infrared (880–920 nm) light off a 30-mm metal cylinder, covered with a reflective tape. When ice is present on the cylinder, the reflectance goes below a threshold that is detected and communicated as a binary output signal. When the output turns high, the sensor also starts its internal heating, melting the ice on the cylinder. When the ice is removed and the reflectance goes above the threshold, the heating is switched off, and a new measurement cycle starts.

As long as all ice is continuously removed, the shape of the instrument will not change during an icing event. The heating will keep the instrument ice-free until it cools down.

The binary output signal is not synchronized. The cycle length is decided by both the time it takes for the ice to change the reflectance of the optical sensor and for the heating to remove the ice. The total time depends on the rate of icing, the type of icing, and the ambient temperature. In order to get a value of the rate of icing, an algorithm that integrates the output signal over 1 min and stores this value every minute can be used. This is illustrated in Fig. 1.

This means that the value will not only indicate when there is ice but also indicate the rate of icing. If the integrated signal is constantly peaking, the instrument could either be malfunctioning or it could mean the icing is so strong that the sensor is unable to remove the ice from the cylinder.

C. Measuring Ice Load

The standard ISO12494 [22] defines ice load as the weight in kg per meter of accumulated ice on different profile dimensions. This is a commonly used definition in estimations of meteorological icing.

The IceMonitor from Combitech AB measures the weight of accumulated ice on a 50-cm-vertical stick, 30 mm in diameter, designed to adhere to ISO12494. The measured weight is scaled to get a value of the ice load. While the IceMonitor can mostly swivel freely, it does not actively rotate. However, when ice accumulates on one side of the stick, the wind may force it to rotate, causing a more evenly distributed ice load.

An advantage with the IceMonitor is its proven reliability of function and sturdy construction.

D. Calculation of Icing Rate by Makkonen

When the size distribution and the concentration of water droplets in a moving air mass are known, it is theoretically possible to calculate the droplets' collision efficiency using fluid dynamics [7], [34], [35]. The LWC and MVD can be used to approximate the values of each individual droplet in these calculations [4], [7].

When the icing process is known, it is possible to calculate the rate of icing, (dM/dt) [6]. The method has been verified in [7], [4], [35], [36], and [2] and has become a standard practice for estimating the icing rate. See the following equation:

$$\frac{dM}{dt} = \alpha_1 \alpha_2 \alpha_3 w v A. \tag{1}$$

M is the mass per meter of the accumulated ice on an infinitely long cylinder. α_1, α_2, and α_3 are different reduction factors, w is the mass concentration of particles, v is the particle velocity, and A is the cross-sectional area. The LWC approximates the mass concentration, and the particles are assumed to have the same velocity as the measured wind speed. We also assume that the icing object is cylindrical and the diameter is constant.

The collision efficiency, α_1, is calculated using constant approximations of the local pressure and temperature. The IceMonitor and the HoloOptics sensor are both cylindrical when ice freezes and have the diameter $D = 30$ mm. The dimensionless parameters K and ϕ are

$$K = \rho_w d^2/(9\mu D) \tag{2}$$

$$\phi = Re^2/K \tag{3}$$

with the density of water $\rho_w = 997$ kg m^{-3}, diameter of the droplets d is approximated by the MVD, the absolute viscosity of air $\mu = 1.7 \times 10^{-5}$ Pas, the Reynolds number $\mathrm{Re} = \rho_a d v/\mu$, and the density of air $\rho_a = 1.1$ kg m^{-3}. These values represent the approximations based on an average barometric pressure at the measurement station. From [7], we get

$$\alpha_1 = A - 0.028 - C(B - 0.0454) \tag{4}$$

where

$$\left.\begin{aligned} A &= 1.066K^{-0.00616}\exp(-1.103K^{-0.688}) \\ B &= 3.641K^{-0.498}\exp(-1.497K^{-0.694}) \\ C &= 0.00637(\phi - 100)^{0.381} \end{aligned}\right\}. \tag{5}$$

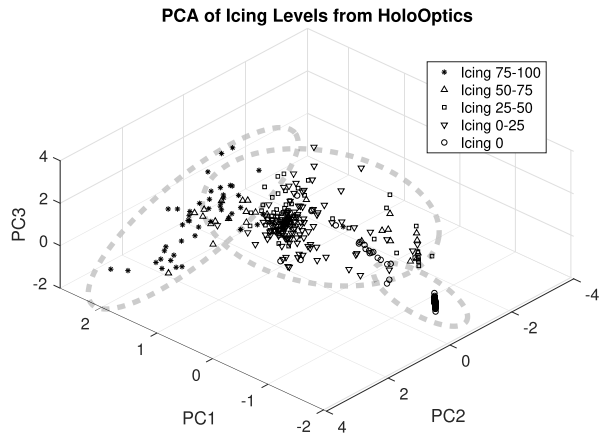

Fig. 2. PCA plot example from Event II. The left dashed ellipse encloses the values with high icing intensity (75–100). The middle dashed ellipse encloses the values with icing intensity between 0 and 75. The right dashed ellipse encloses the values with icing intensity equal to zero.

We set $\alpha_2 = 1$. This means that all particles are assumed to be of liquid water and the water is assumed not to bounce off. Snow or ice particles that contribute to the icing are not included.

$\alpha_3 = 1$ in the case of rime icing, i.e., when all liquid ice freezes upon impact. In the case of glaze icing, i.e., when liquid water is collected on the structure before it freezes, α_3 needs to be reduced since some collected water will run off without freezing.

E. Estimation of Icing Intensity by KNN

Pattern recognition and machine learning are powerful tools used to create algorithms that recognize conditions in complex sets of data. We wanted to estimate the icing rate by using one set of data for training and another set for testing the model; thus, we chose the k-nearest neighbor (KNN) regression for this purpose.

In the estimation of icing intensity, we used three principal components to make the model and five neighbors. Fig. 2 shows a principal component analysis (PCA) from Event II. The training data were used to find the five nearest neighbors for every point in the test data. The variables used were wind speed, LWC, and MVD, and the output was the icing intensity measured by the HoloOptics sensor. Every point in the diagram is a sample of the training data. For illustration, the points have been divided into five bins representing output value ranges. The output when using the test data is the average value of the five closest neighbors of the training data.

In the training and testing of the model, both momentary and/or historical data can be used as input. In the example below, we only use momentary data from November 1, 2018 to November 25, 2018. This means Events I-IX are within the learning data range, whereas Events X-XVI are outside the learning data range.

We want a value of the icing intensity as output. The maximum gradient in the ice load measured by the IceMonitor was 0.2 kg m^{-1} min^{-1}. Since the maximum value from the HoloOptics sensor is 100, we use 0.2/100 as a scaling factor for the KNN model.

F. Simulation of Ice Load From KNN Model

A simulation of the current ice load, $L[n]$ kg m^{-1}, is made heuristically by adding an estimation of the erosion, which is negative, to the intensity of icing and the previous value of the ice load. Equation 6 shows the resulting recursive calculation

$$L[n] = L[n-1] + kI_{KNN}[n] + r[n]. \tag{6}$$

$L[n-1]$ is the previous value of the ice load, and $I_{KNN}[n]$ is the output from the KNN estimation. k is a scaling factor from the intensity value to the ice rate.

The erosion $r[n]$ kg m^{-1} min^{-1} is made heuristically as a function of the accumulated ice load, the wind speed, and the temperature added as a Sigmoid function with a middle point at -2 °C. See the following equation:

$$r[n] = \frac{1}{30e^{-3(T-(-2))}} L[n-1]1.01^{v^2} \tag{7}$$

where T is the temperature and v is the wind speed.

G. SMHI/AROME Predicted Ice Load

The predicted ice load is based on the predicted values of the LWC and the MVD, as well as other meteorological parameters included in the Application de la Recherche À l'Opérationnel À Méso Echelle (AROME) numerical weather prediction (NWP) model [27], [37], [38]. The NWP model data are provided by the Swedish Meteorological and Hydrological Institute (SMHI). The NWP model makes high-resolution predictions based on observations and historical data. Normally, this model has a 2.5-km horizontal resolution, but for this study, SMHI ran a special model domain locally with a 500-m resolution.

SMHI did not fully implement the erosion/ablation for this article. Therefore, the predicted ice load is set to zero every 6 h starting from 00:00 (e.g., 00:00 and 06:00). The prediction is based on the weather parameters' average during the last 10 min before every whole hour.

H. Installation

Fig. 3 shows the installation. The two camera houses of the DII are placed on top. The smaller CDP is just below together with the HoloOptics sensor. These instruments are mounted on a rotating mast to follow the horizontal direction of the wind.

The Eolos weather sensor is seen to the far right, mounted on a horizontal boom. The IceMonitor is visible in the middle.

III. Results

From the beginning of November 2018 until the end of February 2019, we identified 12 icing events and four icing events by the end of February 2019. The events lasted from a few hours up to weeks. See Tables I and II. One event was the period from when the HoloOptics sensor was active, or the IceMonitor registered some ice load until the ice load reached zero or almost zero again.

In the time left between the events in Tables I and II, there was no or almost no icing. A selection of these events is shown here, but all events were analyzed. We focused on the result

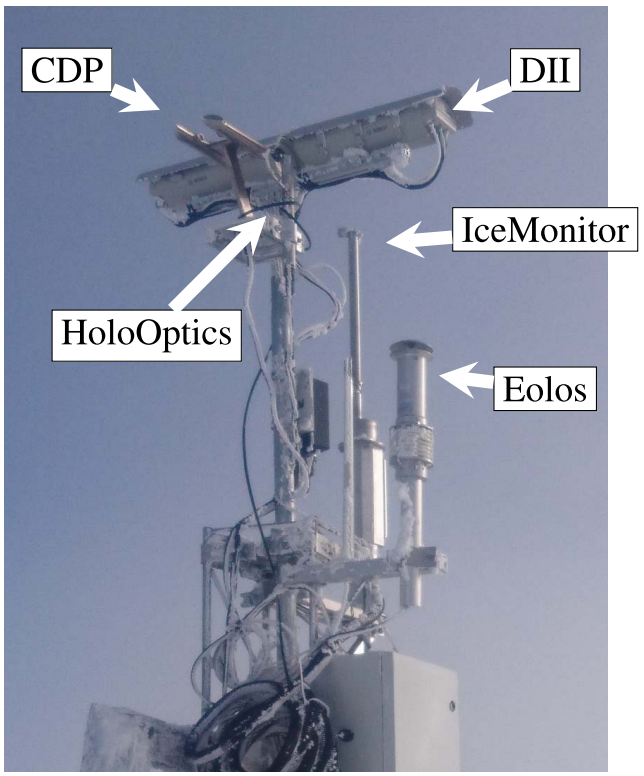

Fig. 3. Image of the complete installation on top of Åreskutan.

TABLE I
SUMMARY OF ICING EVENTS FROM NOVEMBER 2, 2018 TO DECEMBER 31, 2018

Event	Start/Stop Time (UTC+01)	Duration (h:min)
I	2018-11-01T19:45/02T04:00	8:15
II	2018-11-02T04:40/11:42	7:02
III	2018-11-02T11:44/15:40	3:56
IV	2018-11-02T15:49/03T22:26	30:37
V	2018-11-07T21:06/08T04:06	7:00
VI	2018-11-09T21:06/10T18:15	21:09
VII	2018-11-11T12:25/14T10:30	70:05
VIII	2018-11-17T05:00/18T19:24	38:24
IX	2018-11-22T14:36/19:33	4:57
X	2018-11-22T22:04/12-10T03:22	413:18
XI	2018-12-15T04:55/12-25T18:44	253:49
XII	2018-12-25T18:05/12-31T11:59	137:54

TABLE II
SUMMARY OF ICING EVENTS FROM FEBRUARY 22, 2019 TO FEBRUARY 26, 2019

Event	Start/Stop Time (UTC+01)	Duration (h:min)
XIII	2019-02-22T09:22/18:45	9:23
XIV	2019-02-22T19:55/24T04:30	32:35
XV	2019-02-24T05:35/25T01:42	20:07
XVI	2019-02-25T01:42/26T08:55	31:13

from measurements at the beginning of November 2018 and in February 2019. The acquired data are available at the IEEE Dataport [14].

It was not possible to access the measurement station from November to February. By the end of December, the whole system broke down. In February, the instruments were cleaned, and some of the equipment were repaired. Unfortunately, due to extreme ice load, the DII gave out due to cable breakage and

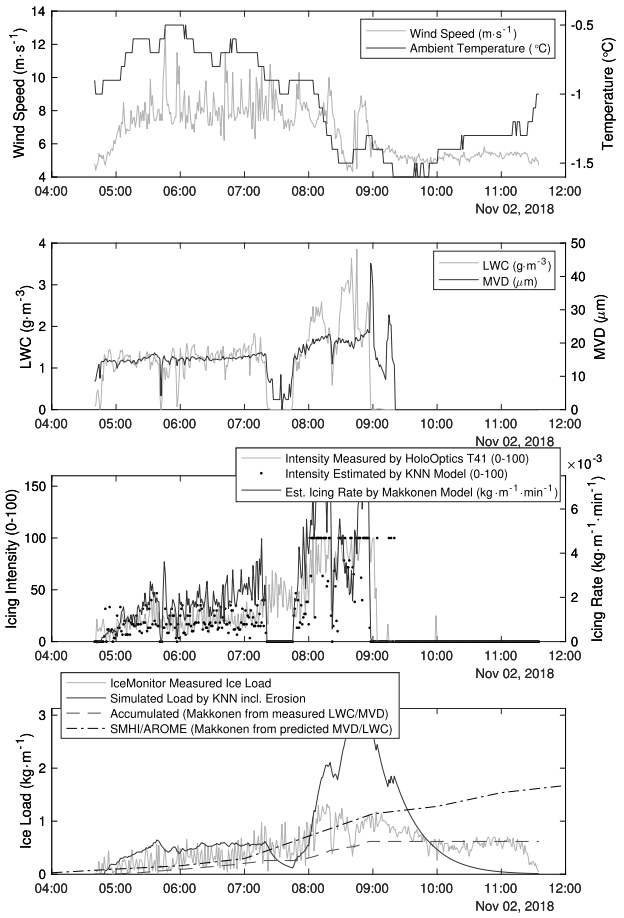

Fig. 4. Plot showing icing Event II.

computer failure, while the HoloOptics sensor was degraded due to the loss of the reflective tape. Therefore, the HoloOptics value from 2019 shows a different characteristic than that previously recorded in 2018. The IceMonitor quickly accumulated more than 10 kg of ice in February, which remained until the end of April. We did not analyse the icing in January and the beginning of February, March, and April 2019.

For November 2018 (Events I-IX), the result can be compared with the estimated ice load from SMHI based on predicted LWC and MVD data from the AROME NWP model.

A. Event II

Fig. 4 shows an icing event on November 2, 2018. The LWC was very high from 04:40 to 09:00. The icing continued sporadically until all the ice melted away at 11:36. Fig. 5 shows a scatterplot of the HoloOptics value versus the calculated icing rate shown in the top diagram in Fig. 4. A polynomial fit to the values that are nonzero in Fig. 5 results in an approximately linear function with $k = 4.7 \times 10^{-5}$. If the same scaling factor is used as in the ice simulation described in Section II-D, $k = 4.7 \times 10^{-5}/0.002 = 0.0024$.

The ice load data from SMHI suggested an increase during the whole event with a small acceleration between 07:00 and 09:00.

B. Event III

Event III on November 2, 2018 started at 11:44 and ended at 15:40. It could be seen as several events as the ice load

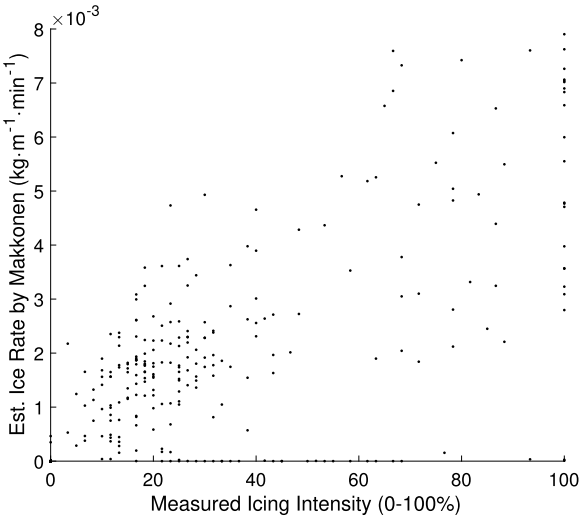

Fig. 5. Plot showing the icing rate calculated using the Makkonen formula versus the icing intensity measured by HoloOptics T41 in Event II.

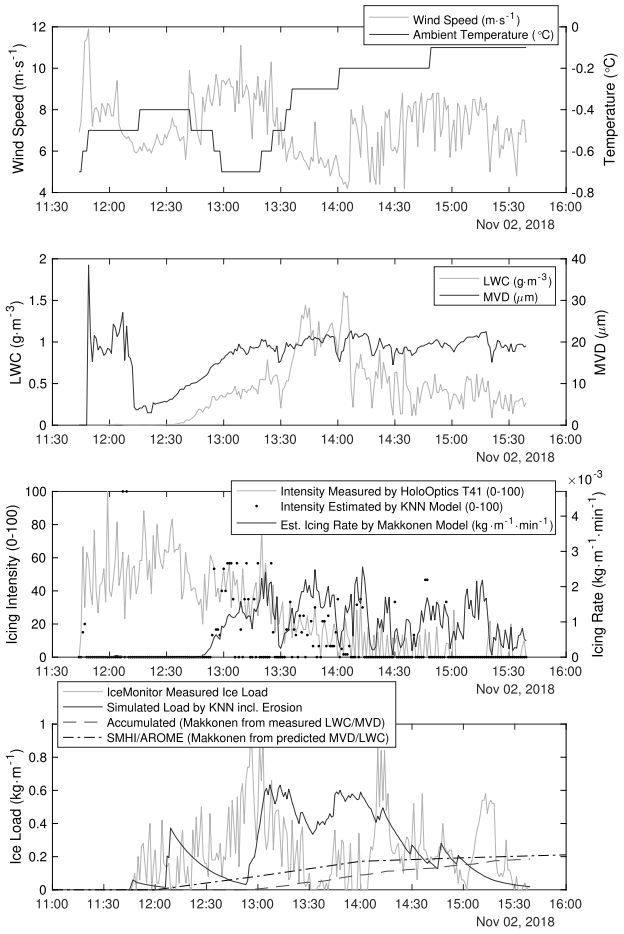

Fig. 6. Plot showing icing Event III.

reached zero several times. The icing of the IceMonitor, as well as the HoloOptics, started at 11:44 when the measured LWC was zero. The LWC did not increase until 1 h later, at 12:40, and shortly after, so did the calculated icing rate.

The SMHI ice load in Fig. 6 was set to zero at 12:00.

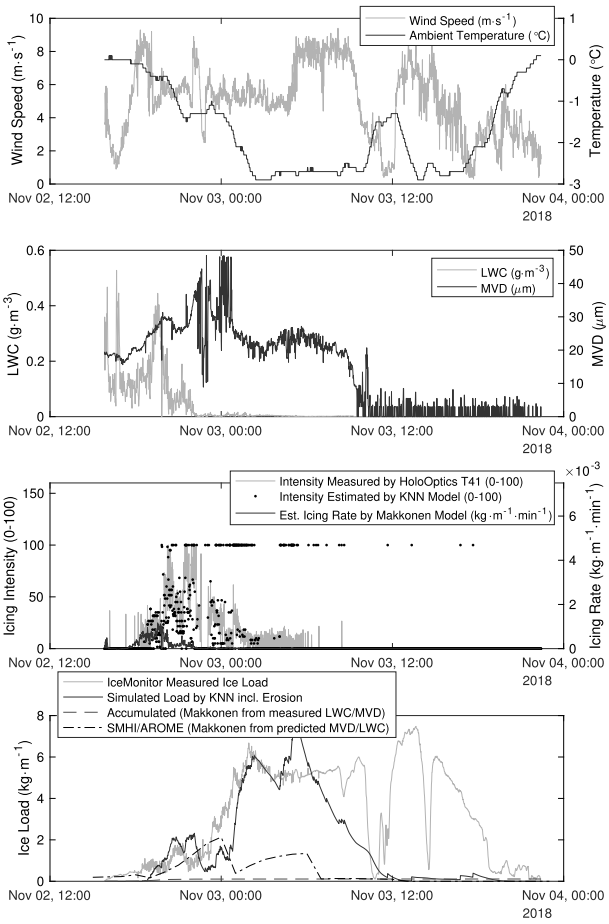

Fig. 7. Plot showing icing Event IV.

C. Event IV

Event IV was longer than the previous events. It illustrates the difficulty at certain times to value the data (see Fig. 7).

The measured ice load remained high until November 3, 2018 T10:00 when there was a dip for about 2 h until the value rose quickly to the previous one and slightly above. At 14:00, there was another dip for 1 h. Then, the value decreased slowly to zero at 22:36.

The predicted ice load from SMHI was reset every 6 h.

D. Event XIII

Event XIII on February 22, 2019 started with a measured ice load of 0.2 kg m^{-1}. At 11:20, the ice load goes down to almost zero and continues to rise until around 16:30. Fig. 8 shows the whole event. Fig. 8 also shows a simulated ice load, described in Section IV.

IV. Discussion and Analysis

A. Measuring MVD and LWC

Both the DII and the CDP have their drawbacks. A systematic difference in LWC and MVD, similar to the previously noticed [27], was also observed in this study. When zeros are removed in the MVD measurement, the mean quote between the DII MVD and the CDP MVD during one Event VII is 0.91, i.e., the DII MVD is 9% lower than the CDP MVD, despite its larger diameter range (see Fig. 9).

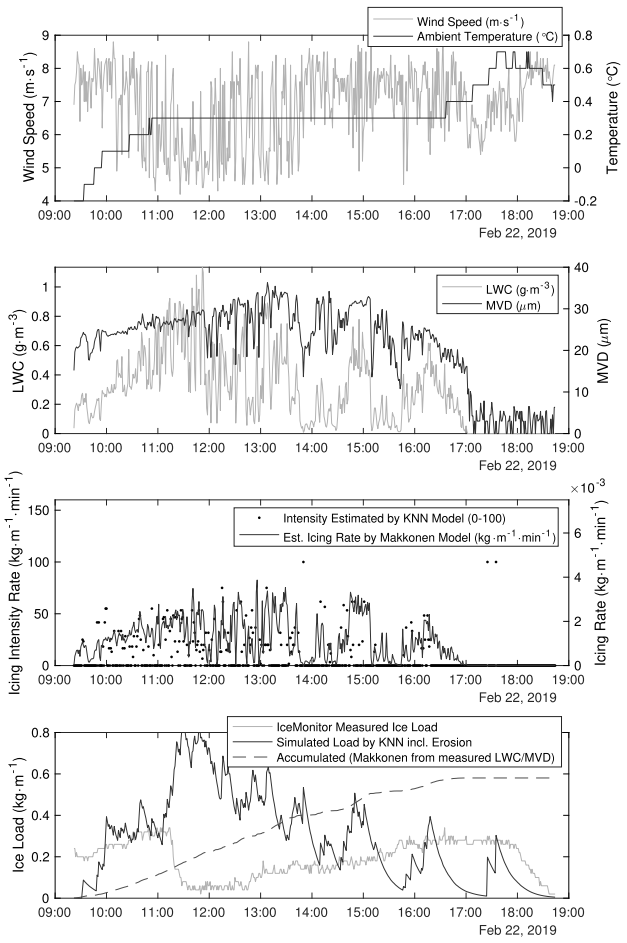

Fig. 8. Plot showing icing Event XIII.

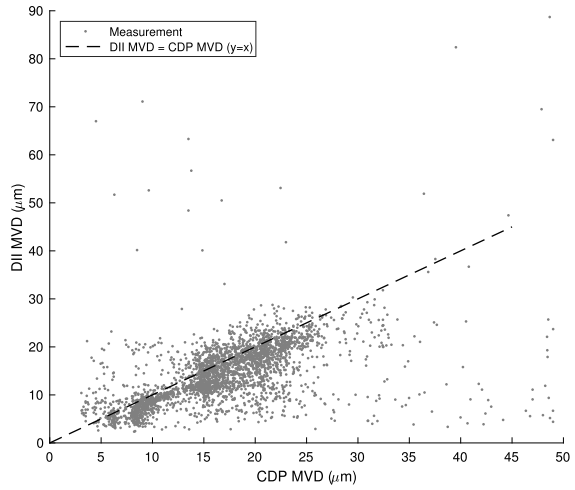

Fig. 9. MVD measured by the DII versus CDP. The dashed line denotes unity.

The CDP heating seems to be efficient to prevent icing from hindering the measurement. However, water on the lenses can affect the measurement significantly. The DII has a quite narrow path between the two camera housings that the air needs to pass through to be measured. A small amount of ice or snow can hinder the air from passing freely, thereby changing the droplet concentration and size distribution of the measured air mass.

The processing speed of the DII depends on the power of the processing computer and the efficiency of its algorithms. Ideas to increase the speed have been presented, but not implemented. Therefore, the sample volume per time unit of the DII is much slower than that of the CDP. This can be an issue when the MVD is large, as the number concentration decreases. This could explain the large difference in both LWC and MVD, e.g., from November 12, 2018 T19:00 to 00:00 (in Event VII). It also means that the MVD/LWC value measured by the DII when the droplet concentration is low will be zero as no droplets are found and measured. The calculated LWC will also not be correct in these cases.

We believe that obstructions in the optical path were the most common cause of errors in the presented study. When ice or snow completely blocked the laser of the CDP or the gap between the illumination and the camera of the DII, the instruments probably did not measure correctly. When the lenses were partly covered, the detection rate was reduced. The measured particle size may also possibly have been affected.

B. Measuring Ice Load

When icing occurs, the ice will accumulate and result in an increased load on the exposed structure. The load can be caused by both atmospheric icing and precipitation. As previously mentioned, we did not have any instrument to measure the precipitation. This can explain why the ice load sometimes increased without measuring atmospheric icing.

From theoretical calculations of the heat balance, there could be a film of water covering the stick before it eventually freezes [6]. There would then be a run-off of water from the stick after a quick collection of water droplets.

Very often, supercooled liquid water droplets coexist with ice crystals in varying concentrations [39].

When estimating the ice load, one has to consider the erosive part of the process. If we make a very simple heuristic model of wind erosion and use the HoloOptics sensor as a measure of the icing intensity, a simulation of ice load can look like Fig. 4. Without adding the erosion, the ice load would only increase above the average. This leads to the question if the empirical adjustments of the Langmuir and Blodgett theory [34], [35], used in the Makkonen formula [7], are correct when the process is seen in a higher temporal resolution.

There were icing events where the icing rate was slow, but the ice remained longer, like in Events IX, X, XII, XIII, and XIV or combinations of slow and quick icing.

Since IceMonitor measures all types of icing, it is somewhat challenging to make an efficient filter function that works in all conditions. The HoloOptics sensor possibly operates differently in that it activates its heating which actively removes the ice as soon as it appears. Therefore, it cannot be expected to detect the slow type of icing that remains longer. This was confirmed in Events IX, X, XII, XIII, XIV, and XV. In Event XI, there was an indication from the HoloOptics sensor at the beginning each icing, but no indication in the middle section when the LWC was higher.

The ice load depends on the intensity of icing as well as historical data since already accumulated ice will change the

shape of the icing object. The shape and type of accumulated ice will also affect the amount of ice eroded due to wind, temperature, etc. Therefore, it is very difficult to predict the specific ice load.

In December, the instruments became more or less covered with ice and snow, affecting the counting of particles and the anemometer primarily.

Variations in the value from the IceMonitor could be caused by spatial variations in the cloud MVD/LWC in combination with wind erosion.

For the load cell of the IceMonitor to work, it must be free to push the load cell down when the ice load increases. There have been concerns that ice could jam the instrument, so it measures zero or very low values. Therefore, it is equipped with heating to prevent the load cell from freezing. There still may be cases when the heating is not enough, making the measured load appear as an inverted transient in the ice load curve.

C. Predicted Versus Measured Ice Load

The ice load estimated and provided by SMHI is based on the predicted values of LWC/MVD and wind speed in the last 10 min of every whole hour, used with the Makkonen formula. By taking the wind speed, MVD, and LWC from SMHI/AROME NWP as input to 1, we get the same ice rate and load. However, measuring icing at the minute level using the IceMonitor reveals a more complex and faster process. The measured LWC also differs significantly from the predicted LWC.

The SMHI/AROME NWP model differs the most from the measured ice load in situations with low LWC or high MVD. Although sublimation and wind erosion are included in the prediction, it does not seem to predict the ablation completely.

The estimated icing rate is based on the Makkonen formula and the assumption that all ice is caused by supercooled liquid water droplets as described in Section II. This is known as rime icing [7]. We had no instrument to measure the precipitation in Åreskutan, so we could not include this in the equation. Had we done so, there might have been a better correlation between the calculated ice rate and the ice rate measured by the IceMonitor.

D. Measuring Icing Intensity

Using the described method of time integration of the digital output and a 1-s sample period, HoloOptics T41 can be used to indicate the intensity level of icing. This works fine in light- and moderate-icing scenarios.

The HoloOptics sensor is generally heated, meaning that the stick will be dry most of the time. Therefore, we would expect the result from the measurement with the HoloOptics sensor to correlate better with the estimated icing intensity according to the assumptions in Section II-D, where we set $\alpha_3 = 1$.

In harsh conditions, the reflective tape may break, causing instrument failure.

E. Temporal Resolution and Correlation

The fast changes in the ice load in some parts of the events could perhaps be interpreted as noise in the measurement, induced by factors such as varying wind speed. However, due to the strong correlation between the instruments seen in Event II (Fig. 1), we believe that there are cases with a high icing rate, but when the ice also erodes equally fast. The wind or water run-off could also cause erosion, which likely happens only when certain conditions are fulfilled, for example, in Events I-III and at the beginning of Events IV-VI. An increased correlation between the measured ice load, the icing intensity, and less noise may be achieved by using the average ice load per minute, instead of the current solution using the last 10-s average reading.

The highest correlation coefficient between the HoloOptics values and calculated icing rate (based on MVD/LWC values from the CDP) was 0.77 in Event II. In other events, the correlation was below 0.5 and even zero (no correlation) in some events. Accumulated ice on the instruments was likely the leading cause for the noncorrelation.

With the method mentioned in Section II-B, the value of icing intensity from 0 to 100 calculated from the HoloOptics sensor should reflect the average icing intensity during the observed minute if a measurement cycle of the sensor is 1 min or shorter. If the cycle is longer, the relation will not work. A solution to this sample problem could be to increase the heating effect of the HoloOptics sensor, thereby decreasing the cycle time, or to find a different, faster method to remove the ice from the sensor. Another solution may be to use two or more sensors that work in parallel. When cycles are overlapping, a higher temporal resolution can be achieved.

TABLE III

ERROR IN THE ESTIMATED ICING INTENSITY (0–100) USING A KNN MODEL DEPENDING ON THE AMOUNT OF INPUT. ABSOLUTE ERROR IS THE MEAN ABSOLUTE ERROR IN PERCENTAGE POINTS DURING THE TESTED EVENT, AND F.I. RATIO IS THE NUMBER OF FALSE INDICATIONS DIVIDED BY THE NUMBER OF CORRECT INDICATIONS

Training Input	Test Data	Absolute Error	F.I. Ratio
Event III	Event II	20.9	64/249 = 0.26
Event III+IV	Event II	17.1	4/227 = 0.02
Event II	Event III	21.9	38/117 = 0.33
Event II+IV	Event III	22.2	12/78 = 0.15
Event II	Event IV	34.5	499/101 = 4.94
Event III	Event IV	30.9	1131/489 = 2.31
Event II+III	Event IV	8.9	54/102 = 0.53

F. Analysis of Result Using KNN

In the following comparison, the output calculated by HoloOptics was used as a measure of the icing intensity. The momentary values of ambient temperature, wind speed, LWC, and MVD are used as input. The error is calculated as the mean difference between estimated and measured output values, from 0 to 100.

In some cases, it may be equally important to know that there is no icing. The false indication ratio (F.I. ratio) is the number of values that are nonzero when they should be zero according to the measurement divided with the number of correct indications, i.e., when the value is nonzero when it should be nonzero. Table III lists these results.

If Event II is used for training and Event IV is used for testing, the KNN model results in a mean absolute error

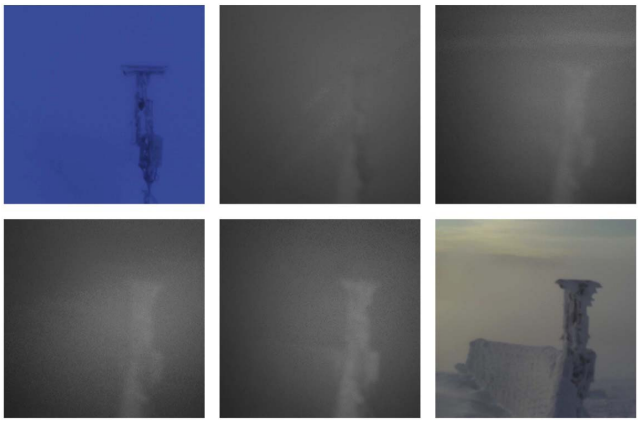

Fig. 10. Sequence of images showing the icing on November 2, 2018. The first image is at 15:45, and the next images are at 16:45 and 17:45 (from top left to right). The bottom left image is taken at 18:45, the middle is taken at 19:45, and the last image (bottom right) is taken at 09:05 the morning after.

of 34.5% points. The F.I. ratio is 4.94. If Event III is used for training and applied to Event IV, the error is 30.9% points, and the F.I. ratio is 2.31. When both Events II and III are used for training, the error in Event IV is only 8.9% points, and the F.I. ratio decreases to 0.53.

In general, the more the data used for training, the better the model becomes at estimating other sequences, and the closer the training data to the testing data in time, the better is the estimation.

This pattern was repeated when applied on Events V, VI, and so on although the result sometimes was less reliable as the instruments were affected by accumulated ice and snow in later events. If enough training data are collected, machine learning algorithms can be used to create a model to estimate the icing rate from a limited set of parameters.

G. Visual Verification of Icing Conditions

Visual observations were used to verify the presence of fog or ice on the instruments. A heated video supervision camera was placed approximately 20 m from the measurement station to give real-time images of the instrument status. The images in Fig. 10 are taken during Event IV, November 2, 2018. During ice accumulation, the visibility is very low, and during nighttime, the lighting is limited to the built-in infrared spotlight. Therefore, it is difficult to measure the exact volume of ice on the instruments from these images.

H. Uncertainties in Droplet Measurement

While the droplet sizes can be measured with good accuracy using shadowgraphy [12], the measurement volume is more difficult to define. However, in a closer investigation of the systematic difference [28], it was found that the resulting error, on average, would not be more than 4% with the DII. A more likely error source would be the differences in the aerodynamic shape of the instruments and the fact that the CDP is designed for use with higher particle velocities. In the field study [27], we could not find any of the expected correlations between wind speed and difference in the measured LWC. The cause of the systematic difference between the DII and CDP is, therefore, still unknown.

Some of the known limitations and uncertainties of the CDP should be mentioned. First of all, the most obvious is that the CDP only measures droplets from 2 to 50 μm in diameter. This article, as well as previous measurements, shows that large droplets are common and will have a strong impact on icing. The CDP only works correctly when the flow of measured particles is perpendicular to its measuring laser beam. This means that the unit needs to be directed toward the wind. If the wind direction varies faster than the motor that can turn the instrument, the measurement will be affected negatively.

There are also uncertainties in single-particle scattering probes such as bin sizing uncertainty due to the Mie scattering pattern, deviations from spherical particle shape, and particle coincidence [10], [40].

I. Coincidence Errors

Coincidence errors may contribute to the 20%–25% error in MVD observed in previous studies [33]. Coincidence errors occur when two particles interfere in one measurement, and the error increases with the number concentration of droplets. Lance [33] demonstrated that the coincidence error leads to a 90% bias in LWC at 400 cm^{-3} from only 10% bias at 100^{-3}.

The number concentration of droplets observed in Åreskutan by the CDP during icing was frequently more than 600^{-3} and occasionally reached higher than 1000^{-3}. Therefore, the LWC value based on the droplet observations by the CDP was likely larger than the actual LWC. Instruments based on a single-particle measurement should consider high concentration.

Also, in measurements with varying concentrations, the coincidence error should be higher than in measurements with constant concentrations, given the same MVD and LWC.

V. Conclusion

The Makkonen model is suitable for estimating icing in 1-h temporal resolution using *in situ* measurements of weather parameters. With a 1-min temporal resolution, the erosion/ablation needs to be modeled more accurately and included.

A KNN model created from the multivariate data analysis, together with a heuristic model of erosion, can be used to simulate the ice load from weather parameters with a 1-min temporal resolution. By using a 7-h-long icing event (Event II) to create the model of the icing intensity, the average error is 21% points when tested on a 4-h event (Event III), and 35% points when tested on a 31-h long, more complex event (Event IV). When both Events II and III were used for training, the error when the model was tested on Event IV was only 8.9% points, and the F.I. ratio decreases to 0.53. In other words, the more the data used for training, the better is the estimation.

Measurements of any kind are difficult in icing conditions, and optical instruments are particularly sensitive. Electrically powered heating is indispensable for keeping the optical parts free from ice. Any moving parts are prone to failure.

The CDP can be used to measure the MVD and LWC in most cases, but it requires to be directed toward the wind,

as well as an accurate and simultaneous measurement of the wind speed. If the wind speed is very low or the direction changes quickly, the measurement becomes unreliable. When ice, water, or dirt comes into contact with the lenses, it will affect the measurement, in particular, the LWC, as few particles will be measured. It is difficult to verify its current condition.

The DII, with its current physical design, is not suitable for the strong icing conditions experienced at Åreskutan. The main problems are the snow that covers the inlet between the two camera houses and cables breaking due to icing. Like the CDP, it needs to be oriented in the direction of the wind. As in the previous studies, we noticed a systematic difference in LWC between the CDP and DII.

Future measurements and development of icing models should consider that a temporal resolution of 1 min or higher is needed to capture and understand the icing process.

ACKNOWLEDGMENT

The authors would like to give special thanks to Esbjörn Olsson, Swedish Meteorological and Hydrological Institute (SMHI, Sundsvall, Sweden), for providing high-resolution numerical weather prediction (NWP) data, and Patrik Jonsson, Björn Ollars, and Olof Carlsson, Combitech AB, Östersund, Sweden, for the physical integration of the instruments and the data gathering. This article presents the verification of correlations between measured meteorological parameters in relation to structural icing. The measurements were recorded on top of Åreskutan, in co-operation with Skistar AB, Åre, Sweden, and the instruments were integrated with the support from Combitech AB.

REFERENCES

[1] N. Davis, A. N. Hahmann, N.-E. Clausen, and M. Žagar, "Forecast of icing events at a wind farm in Sweden," *J. Appl. Meteorol. Climatol.*, vol. 53, no. 2, pp. 262–281, Feb. 2014.

[2] J. Yang, W. Yu, J. Choisnard, A. Forcione, and S. Antic, "Coupled atmospheric–ice load model for evaluation of wind plant power loss," *J. Appl. Meteorol. Climatol.*, vol. 54, no. 6, pp. 1142–1161, Jun. 2015, doi: 10.1175/jamc-d-14-0125.1.

[3] S. Dierer, R. Oechslin, and R. Cattin, "Wind turbines in icing conditions: Performance and prediction," *Adv. Sci. Res.*, vol. 6, no. 1, pp. 245–250, Sep. 2011.

[4] D. M. L. Dobesch and H. Nikolov, *Physical Processes, Modelling and Measuring of Icing Effects in Europe* (Österreichische Beiträge zu Meteorologie und Geophysik), vol. 415, no. 34. Vienna, Austria: Zentralanstalt für Meteorologie und Geodynamik, 2005.

[5] L. Makkonen, "Estimating intensity of atmospheric ice accretion on stationary structures," *J. Appl. Meteorol.*, vol. 20, no. 5, pp. 595–600, May 1981.

[6] L. Makkonen, "Modeling of ice accretion on wires," *J. Climate Appl. Meteorol.*, vol. 23, no. 6, pp. 929–939, Jun. 1984.

[7] L. Makkonen, "Models for the growth of rime, glaze, icicles and wet snow on structures," *Philos. Trans. Roy. Soc. London A, Math., Phys. Eng. Sci.*, vol. 358, no. 1776, pp. 2913–2939, Nov. 2000.

[8] J. Molinder, H. Körnich, E. Olsson, H. Bergström, and A. Sjöblom, "Probabilistic forecasting of wind power production losses in cold climates: A case study," *Wind Energ. Sci.*, vol. 3, no. 2, pp. 667–680, Oct. 2018.

[9] P. Thorsson, S. Söderberg, and H. Bergström, "Modelling atmospheric icing: A comparison between icing calculated with measured meteorological data and NWP data," *Cold Regions Sci. Technol.*, vol. 119, pp. 124–131, Nov. 2015.

[10] D. Baumgardner *et al.*, "AMS meteorological monographs, ice formation and evolution in clouds and precipitation: Measurement and modeling challenges," in *Cloud Ice Properties: In Situ Measurement Challenges*, vol. 58. Providence, RI, USA: AMS, Jan. 2017, ch. 9, doi: 10.1175/amsmonographs-d-16-0011.1.

[11] R. Cattin and D. Heikkilä, "Evaluation of ice detection systems for wind turbines," Meteotest, Bern, Switzerland, Tech. Rep., 2016.

[12] S. Rydblom and B. Thornberg, "Liquid water content and droplet sizing shadowgraph measuring system for wind turbine icing detection," *IEEE Sensors J.*, vol. 16, no. 8, pp. 2714–2725, Apr. 2016.

[13] S. Rydblom and B. Thörnberg, "Droplet imaging instrument metrology instrument for icing condition detection," in *Proc. IEEE Int. Conf. Imag. Syst. Techn. (IST)*, Oct. 2016, pp. 71–76.

[14] S. Rydblom. (2019). *Are1819*. [Online]. Available: https://ieee-dataport.org/open-access/are1819, doi: 10.21227/nf2s-h782.

[15] R. E. Bredesen *et al.*, "IEA wind recommended practices 13, edition 2: Wind energy projects in cold climates," Int. Energy Agency, Paris, France, IEA Wind, Tech. Rep., 2017.

[16] V. Lehtomäki *et al.*, "Iea wind task 19 wind energy in cold climates, available technologies for wind energy in cold climates," 2nd ed. Int. Energy Agency, Paris, France, Tech. Rep., 2018.

[17] W. Jasinski, S. Noe, M. Selig, M. Bragg, W. Jasinski, S. Noe, M. Selig, and M. Bragg, "Wind turbine performance under icing conditions," in *Proc. 35th Aerosp. Sci. Meeting Exhibit*, 1997, p. 977.

[18] M. C. Homola, T. Wallenius, L. Makkonen, P. J. Nicklasson, and P. A. Sundsbø, "Turbine size and temperature dependence of icing on wind turbine blades," *Wind Eng.*, vol. 34, no. 6, pp. 615–627, Dec. 2010.

[19] A. Hudecz, H. Koss, and M. O. L. Hansen, "Ice accretion on wind turbine blades," in *Proc. 15th Int. Workshop Atmospheric Icing Struct. (IWAIS)*, 2013.

[20] L. Makkonen, T. Laakso, M. Marjaniemi, and K. J. Finstad, "Modelling and prevention of ice accretion on wind turbines," *Wind Eng.*, vol. 25, no. 1, pp. 3–21, Jan. 2001.

[21] G. Fortin and J. Perron, "Wind turbine icing and de-icing," in *Proc. 47th AIAA Aerosp. Sci. Meeting Including New Horizons Forum Aerosp. Expo.*, Jan. 2009, p. 274.

[22] *Atmospheric Icing of Structures*, Standard ISO 12494, 2001.

[23] O. Fakorede, Z. Feger, H. Ibrahim, A. Ilinca, J. Perron, and C. Masson, "Ice protection systems for wind turbines in cold climate: Characteristics, comparisons and analysis," *Renew. Sustain. Energy Rev.*, vol. 65, pp. 662–675, Nov. 2016.

[24] O. Parent and A. Ilinca, "Anti-icing and de-icing techniques for wind turbines: Critical review," *Cold Regions Sci. Technol.*, vol. 65, no. 1, pp. 88–96, Jan. 2011.

[25] C. Hochart, G. Fortin, J. Perron, and A. Ilinca, "Wind turbine performance under icing conditions," *Wind Energy, Int. J. Prog. Appl. Wind Power Convers. Technol.*, vol. 11, no. 4, pp. 319–333, 2008.

[26] O. Fakorede, H. Ibrahim, J. Perron, and A. Ilinca, *Modelling Ice Accretion and its Effects on Wind Turbine Blades*. Hauppauge, NY, USA: Nova Publisher, Jan. 2013.

[27] S. Rydblom, B. Thornberg, and E. Olsson, "Field study of LWC and MVD using the droplet imaging instrument," *IEEE Trans. Instrum. Meas.*, vol. 68, no. 2, pp. 614–622, Feb. 2019.

[28] S. Rydblom and B. Thörnberg, "Particle measurement volume and light intensity in a shadowgraph imaging system," in *Proc. IEEE Int. Conf. Imag. Syst. Techn. (IST)*, Jan. 2018, pp. 1–4.

[29] D. Baumgardner, "An analysis and comparison of 5 water droplet measuring-instruments," *J. Climate Appl. Meteorol.*, vol. 22, no. 5, pp. 891–910, 1983.

[30] J. E. Dye and D. Baumgardner, "Evaluation of the forward scattering spectrometer probe. Part I: Electronic and optical studies," *J. Atmos. Ocean. Technol.*, vol. 1, no. 4, pp. 329–344, Dec. 1984.

[31] M. Wendisch and J.-L. Brenguier, *Airborne Measurements for Environmental Research: Methods and Instruments* (Wiley Series in Atmospheric Physics and Remote Sensing). Weinheim, Germany: Wiley, 2013.

[32] S. Faber, J. R. French, and R. Jackson, "Laboratory and in-flight evaluation of measurement uncertainties from a commercial cloud droplet probe (CDP)," *Atmos. Meas. Tech.*, vol. 11, no. 6, pp. 3645–3659, Jun. 2018, doi: 10.5194/amt-11-3645-2018.

[33] S. Lance, "Coincidence errors in a cloud droplet probe (CDP) and a cloud and aerosol spectrometer (CAS), and the improved performance of a modified CDP," *J. Atmos. Ocean. Technol.*, vol. 29, no. 10, pp. 1532–1541, Oct. 2012. [Online]. Available: https://journals.ametsoc.org/doi/abs/10.1175/JTECH-D-11-00208.1

[34] I. Langmuir and K. Blodgett, *A Mathematical Investigation of Water Droplet Trajectories*, vol. 196. Program Press, 1945, pp. 348–355.
[35] K. J. Finstad, E. P. Lozowski, and E. M. Gates, "A computational investigation of water droplet trajectories," *J. Atmos. Ocean. Technol.*, vol. 5, no. 1, pp. 160–170, Feb. 1988.
[36] B. E. K. Nygaard, "Evaluation of icing simulations for the cost 727 icing test sites in europe," in *Proc. IWAIS*, Andermatt, Switzerland, 2009.
[37] Y. Seity *et al.*, "The AROME-france convective-scale operational model," *Monthly Weather Rev.*, vol. 139, no. 3, pp. 976–991, Mar. 2011.
[38] L. Bengtsson *et al.*, "The Harmonie–Arome model configuration in the Aladin–Hirlam NWP system," *Monthly Weather Rev.*, vol. 145, no. 5, pp. 1919–1935, 2017.
[39] C. Andronache, *Mixed-Phase Clouds: Observations and Modeling*. Amsterdam, The Netherlands: Elsevier, 2017.
[40] W. A. Cooper, "Effects of coincidence on measurements with a forward scattering spectrometer probe," *J. Atmos. Ocean. Technol.*, vol. 5, no. 6, pp. 823–832, Dec. 1988.

Stefani Rydblom (Member, IEEE) received the M.S. degree in applied physics and electrical engineering from Linköping University, Linköping, Sweden, in 2001, and the Ph.D. degree from Mid Sweden University, Sundsvall, Sweden, in 2019.

From 2002 to 2009, she was with Bombardier Transportation, Västerås, Sweden, where she involved in the design of train control systems and engineering bid management. From 2009 to 2011, she was with Engineering Project Management, Permobil, Timrå, Sweden, and from 2012 to 2013, as a Service Engineer at ABB, Sundsvall, Sweden. She is currently with the RISE Research Institutes of Sweden, Sundsvall. Her research interests include applied measuring techniques and real-time image processing.

Benny Thörnberg received the B.Sc. degree in electrical engineering, and the Licentiate (Tech.) and Ph.D. degrees from Mid Sweden University, Sundsvall, Sweden, in 1988, 2001, 2004, and 2006, respectively.

From 1990 to 1997, he was with Regam Medical Systems AB, Sundsvall, where he was working on the development of a camera design for intraoral X-ray imaging. He is currently an Associate Professor with the Department of Electronics Design, Mid Sweden University. His current research interests include machine vision, metrology, design methods for embedded systems and, in particular, real-time video processing and analysis.